

# Comprehensive application of bioinformatics analysis and experimental exploration identifying miR-34a/CDK6 axis as the key regulators for radiation-induced lung injury progression

W. Wu<sup>1,2#</sup>, X. Zhou<sup>1#</sup>, L. Xiao<sup>3</sup>, P. Bao<sup>3\*</sup>, X. Liu<sup>1\*</sup>

<sup>1</sup>Department of Nuclear Medicine, The Eighth Medical Center of PLA General Hospital, Beijing, China

<sup>2</sup>Graduate School of Hebei North University, Hebei, China

<sup>3</sup>Department of Respiratory and Critical Care Medicine, The Eighth Medical Center of PLA General Hospital, Beijing, China

## ► Original article

### \*Corresponding author:

Pengtao Bao, Ph.D.,  
Xiaofei Liu, Ph.D.,  
E-mail: bao03@163.com,  
liufly301@163.com

Received: December 2022

Final revised: May 2023

Accepted: June 2023

Int. J. Radiat. Res., October 2023;  
21(4): 699-706

DOI: 10.52547/ijrr.21.4.14

**Keywords:** GEO dataset, miRNA, protein-protein interaction, RILI.

#Wenjie Wu and Xiaohong Zhou contribute equal for this work.

## INTRODUCTION

Radiation therapy (RT) is one of the three most effective treatment modalities for tumors, alongside surgery and chemotherapy <sup>(1)</sup>. Radiation-induced lung injury (RILI) encompasses various pulmonary toxicities resulting from RT, with acute manifestations, such as pneumonia, and chronic manifestations, including pulmonary fibrosis <sup>(2-3)</sup>. RILI currently affects approximately 5–20% of patients and serves as a risk factor for tumor recurrence <sup>(4)</sup>, making the development of effective prevention and treatment strategies for RILI essential to enhance the prognosis of patients undergoing RT <sup>(5)</sup>.

Understanding the pathogenesis of RILI is critical for the advancement of therapeutic approaches. The availability of RNA sequencing (RNA-Seq) data in public databases has grown rapidly in recent years. By utilizing bioinformatics analysis, the raw data of

## ABSTRACT

**Background:** The pathogenesis of radiation-induced lung injury (RILI) remains elusive. In this study, we aimed to elucidate the mechanism underlying RILI progression by employing a comprehensive approach, integrating bioinformatics analysis and experimental validation. **Materials and Methods:** Raw transcriptome sequencing data from two Gene Expression Omnibus (GEO) datasets, GSE202586 and GSE14431, were downloaded and overlapping genes were identified. Differential expressions of microRNAs (miRNAs) were analyzed using GEO2R software on the GSE202586 dataset. The miRDB database and miRWalk database were utilized to identify miRNA targets. Specific miRNA inhibitors or protein siRNA were administered to RILI mouse models for experimental confirmation. **Results:** Ten genes were consistently upregulated in the RILI groups across both datasets. A series of miRNAs were dysregulated in the RILI group, with miR-34a exhibiting the largest difference. By integrating target exploration and protein-protein interaction (PPI) analysis, we determined that the miR-34a/CDK6 axis may be the key regulator of RILI progression. Notably, miR-34a inhibitor treatment significantly alleviated alveolitis in RILI mice, and this effect was substantially reversed by CDK6 siRNA. **Conclusion:** Targeting the miR-34a/CDK6 axis presents a potential therapeutic strategy for RILI.

RNA-Seq can be mined to provide a powerful tool for the in-depth examination of pathological mechanisms <sup>(6)</sup>. The mouse model is a widely used instrument for studying RILI <sup>(5)</sup>, with numerous RNA-Seq datasets based on the RILI mouse model accessible in public databases <sup>(7)</sup>, such as the Gene Expression Omnibus (GEO). Upon reviewing the GEO dataset, we identified dataset GSE202586 and GSE14431, both containing raw transcriptome sequencing data from RILI mouse models with varying radiation doses and exposure durations.

MicroRNAs (miRNAs) are functional regulators of gene expression at the transcriptional and post-transcriptional levels <sup>(8-9)</sup>. The role of miRNA regulation in RILI pathogenesis has been extensively investigated in recent years <sup>(9)</sup>. In our previous research, we discovered that a specific miRNA, miR-21, could modulate RILI by affecting macrophage function <sup>(5)</sup>. As the pathogenesis of RILI involves a synergistic process of multiple molecules, further

exploration of the regulatory effects of microRNAs and their targets on RILI is warranted

GSE202586 also includes miRNA data on aberrant expression in RILI mice. These open data resources facilitate a deeper investigation into the interaction network of microRNA-targets and the elucidation of previously unknown molecular mechanisms.

In this study, we employed a combination of bioinformatics analysis and experimental investigation to identify the overlapping transcripts between GSE202586 and GSE14431, as well as the dysregulated miRNAs in GSE202586. We uncovered the role of miR-34a in regulating RILI. The novel finding of this study is the determination that miR-34a can form an interaction network with numerous RILI-related proteins, potentially achieved through targeting CDK6.

## MATERIALS AND METHODS

### Bioinformatics analysis

Datasets GSE202586 and GSE14431, derived from *Mus musculus*, were acquired from the GEO database (<https://www.ncbi.nlm.nih.gov/gds/>, USA). The GEO2R tool (<https://www.ncbi.nlm.nih.gov/geo/geo2r/>, USA) facilitated the identification of differentially expressed genes (DEGs). Metascape (<https://metascape.org/>) was employed for bioinformatics analysis, encompassing Gene Ontology (GO) and Kyoto Encyclopedia of Genes and Genomes (KEGG) pathways. Protein-protein interactions of the identified DEGs were analyzed using the Search Tool for the Retrieval of Interacting Genes (STRING) database (<https://string-db.org/>)<sup>(7)</sup>.

### miRNA target prediction

To predict specific miRNA targets, we utilized miRDB (<https://mirdb.org/>)<sup>(8)</sup> and miRWalk (<http://mirwalk.umm.uni-heidelberg.de/>)<sup>(9)</sup>. Only genes present in both prediction software were considered as target genes.

### Vectors

Recombinant miR-34a inhibitor adenovirus and CDK6 siRNA adenovirus were synthesized by RiboBio (Guangzhou, China).

### RILI mouse model

The RILI mouse model was established through a single dose of 18 Gy (1.5 Gy/min for 12 min) treatment using an X-ray irradiator (X-RAD 320, USA), as previously reported<sup>(10)</sup>. Mice receiving 0 Gy served as controls. Four weeks post-irradiation, mice were divided into three groups: R group, R-miRi group, and R-miRi-Ci group. The R group did not receive additional treatment; the R-miRi group received miR-34a-inhibitor adenovirus injection via tail vein; the R-miRi-Ci group received both miR-34a-inhibitor adenovirus and CDK6 siRNA adenovirus

injections via tail vein. Mice were euthanized at 4, 8, and 12 weeks post-radiation, with serum and lung tissue samples collected.

### Molecular expression assay

ELISA kits for TNF- $\alpha$  (Catalog #PMTA00B), il-6 (Catalog #PM6000B), and TGF- $\beta$  (Catalog #PDB100C) were procured from R&D Systems (USA). Serum cytokine levels from the mouse model were assessed following the manufacturer's protocol. miRNA and mRNA levels were determined using quantitative reverse transcription-PCR (RT-qPCR) according to our previous report<sup>(5)</sup>.

### Pulmonary interstitial area density (PIAD) determination

PIAD in lung tissue samples was determined following a previously reported method<sup>(10)</sup>. Pathological changes in lung tissue across groups were examined after hematoxylin/eosin (HE) staining. A total of 10 fields per section were randomly selected for statistical analysis. Image Pro-Plus 6.0 software (Media Cybernetics, USA) was employed to calculate PIAD, expressed as the pulmonary interstitial area per  $\times 200$  field.

### Statistical analysis

All statistical analyses were conducted using IBM SPSS software package (version 21.0; USA). Student's t-test was applied for continuous data analysis. Differences with a  $p$ -value  $< 0.05$  were deemed statistically significant.

## RESULTS

### Identification of overlapping transcripts between GSE202586 and GSE14431

The global transcriptome sequencing results of liver and lung tissues in mice after 48 hours of X-ray exposure were mapped in GSE202586. We compared the control group (0 Gy) with the treatment group (8 Gy) in lung tissue. Utilizing  $|\log(\text{fold change})| > 1$  and a  $p$ -value  $< 0.05$ , we identified 53 upregulated and 65 downregulated targets in the treatment group compared to the control group (figure 1A-B). GSE14431 mapped the global transcriptome sequencing results in lung tissues with specific treatment, including a single 25 Gy radiation treatment for six weeks. Comparing the control group with the 25 Gy radiation treated group (treatment group), we identified 55 upregulated and 22 downregulated targets in the treatment group (figure 1C-D). The Venn diagram revealed a small cluster of overlapping targets between the two datasets (10 upregulated cases, figure 1E). The statistical characteristics of the overlapping targets in GSE202586 and GSE14431 are presented in tables 1 and 2, respectively. GO analysis mapped the main biological processes related to the overlapping

targets (figure 1F), indicating their involvement in collagen synthesis and pulmonary fibrosis (figure

1G), consistent with the reported pathogenic phenotype of RILI<sup>(11)</sup>.

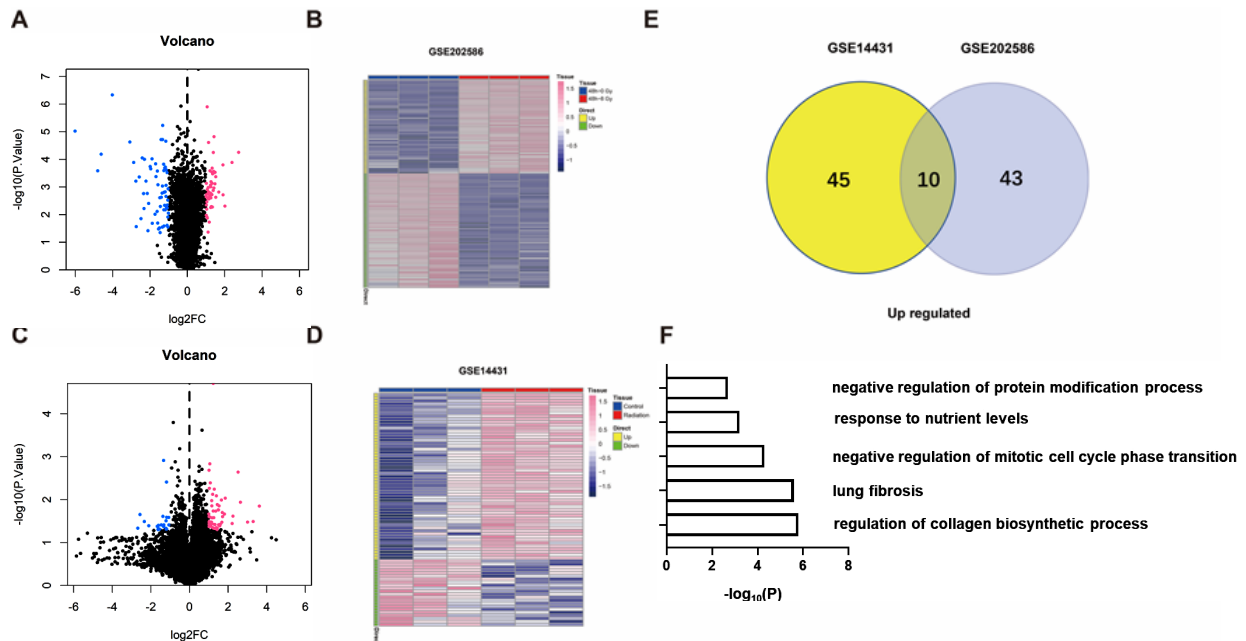


**Figure 1.** Identification of dis-regulated transcripts in response to RILI in mice by using GEO public datasets. **(A)** Volcano plot and **(B)** Heatmap analysis displaying the dis-regulated transcripts in GEO public datasets GSE202586; **(C)** Volcano plot and **(D)** Heatmap analysis displaying the dis-regulated transcripts in GEO public datasets GSE14431; **(E)** Venn diagram showing the overlapped transcripts between GSE202586 and GSE14431; **(F)** The top-level GO biological processes of the differentially expressed transcripts. The plot was calculated and drawn by Metascape Gene List Analysis.

**Table 1.** Ten overlapped targets# and their statistical characteristics& in GSE202586 dataset.

Gene symbol	log (fold change)	t value	P Value	B value
<b>Cdkn1a</b>	2.741778	15.10659	5.60E-05	2.715919
<b>Ctgf</b>	1.23745	7.976742	0.000865	-0.47
<b>Errfi1</b>	1.405892	10.17214	0.000309	0.743734
<b>Fam107a</b>	1.349774	9.983829	0.000335	0.650055
<b>Klf15</b>	1.189115	6.400294	0.002147	-1.54789
<b>Map3k6</b>	1.307423	10.35913	0.000286	0.835078
<b>Mt2</b>	1.682003	6.946874	0.001536	-1.15027
<b>Rgcc</b>	1.51897	9.428677	0.000427	0.363462
<b>Spp1</b>	1.282908	5.13984	0.005139	-2.58262
<b>Tsc22d3</b>	1.325066	11.13969	0.000209	1.199372

#: "Ten overlapped targets" refers to the 10 targets discovered in the Venn diagram in Figure 2E; &: "statistical characteristics" was calculated by student t test, by comparing the control group and treatment group. The control group includes three lung samples harvested 48 h after 0 Gy treatment; The treatment group includes three lung samples harvested 48 h after 8 Gy treatment;

### Identification of dysregulated miRNAs in GSE202586

GSE202586 also mapped the global miRNAs sequencing results. Using GEO2R, we discovered a series of dysregulated miRNAs in the treatment group (table 3, figure 2A). The expression values of the top five miRNAs are displayed in figure 2B-F. The data revealed that mmu-miR-34a-5p had the largest difference and was the only miRNA upregulated in the treatment group (all others were downregulated).

We constructed a RILI mouse model (R group) to validate these findings, excluding mmu-miR-3473g and mmu-miR-6965-5p due to their rarity. The data demonstrated a significant time-dependent increase

**Table 2.** Ten overlapped targets# and their statistical characteristics& in GSE14431 dataset.

Gene symbol	log (fold change)	t	P.Value	B
<b>Cdkn1a</b>	2.210172	2.83726	0.035987	-3.84069
<b>Ctgf</b>	1.019658	2.892624	0.033717	-3.82105
<b>Errfi1</b>	1.196188	2.650914	0.044964	-3.91
<b>Fam107a</b>	3.620685	3.67454	0.014143	-3.58703
<b>Klf15</b>	1.704287	3.348355	0.020083	-3.67529
<b>Map3k6</b>	2.522727	5.680257	0.002286	-3.24923
<b>Mt2</b>	1.232723	15.36987	1.97E-05	-2.93475
<b>Rgcc</b>	1.149877	3.957163	0.010578	-3.52009
<b>Spp1</b>	1.434882	2.630357	0.046096	-3.91795
<b>Tsc22d3</b>	1.05308	6.264121	0.001471	-3.19307

#: "Ten overlapped targets" refers to the 10 targets discovered in the Venn diagram in figure 2E; &: "statistical characteristics" was calculated by student t test, by comparing the control group and treatment group. The control group includes three lung samples harvested 48 h after 0 Gy treatment; The treatment group includes three lung samples harvested 48 h after 8 Gy treatment.

of mmu-miR-34a-5p within 24 weeks post-irradiation (figure 2G, ANOVA:  $p < 0.05$ ). mmu-miR-142a-5p and mmu-miR-142a-3p were also influenced by irradiation, but their expression trends post-irradiation were irregular (figure 2H-I, ANOVA:  $p > 0.05$ ). Additionally, miR-34a was closely related to inflammation and pulmonary fibrosis caused by lung injury<sup>(12-13)</sup>. Consequently, we further investigated the potential roles of miR-34a in RILI.

### Identification of potential miR-34a targets and the associated PPI network

To identify potential targets for miR-34a, we utilized the miRDB and miRWalk databases. In

miRDB, we found 794 targets for miR-34a, while miRWalk presented 2,685 targets. There were 225 overlapping targets between the two databases (figure 3A). We selected the top 50 targets, along with the differentially expressed genes identified in figure 1E, for the PPI analysis. Figure 3B reveals that most of the targets did not interact with other genes, with only two small clusters of genes forming independent PPI networks. Notably, the PPI network centered on CDK6-CDKn1A encompassed the most targets (figure 3B). Since CDK6 is a target of miR-34a<sup>(14)</sup>, we hypothesized that the miR-34a/CDK6-CDKn1A axis may play a crucial role in RILI progression.

To validate these findings, we compared the R group mice with the R-miRi group mice. The miR-34a level in the R-miRi group was lower than that in the R group (figures 3C and 2G), demonstrating the effectiveness of the miR-34a-inhibitor adenovirus in inhibiting miR-34a expression. In the R group, CDK6 levels decreased while CDKn1A levels increased in a time-dependent manner within 24 weeks post-irradiation, indicating an association between the CDK6/CDKn1A axis and RILI progression. In the R-miRi group, CDK6 levels increased and CDKn1A levels decreased compared to the R group, suggesting that miR-34a targets the CDK6/CDKn1A axis.

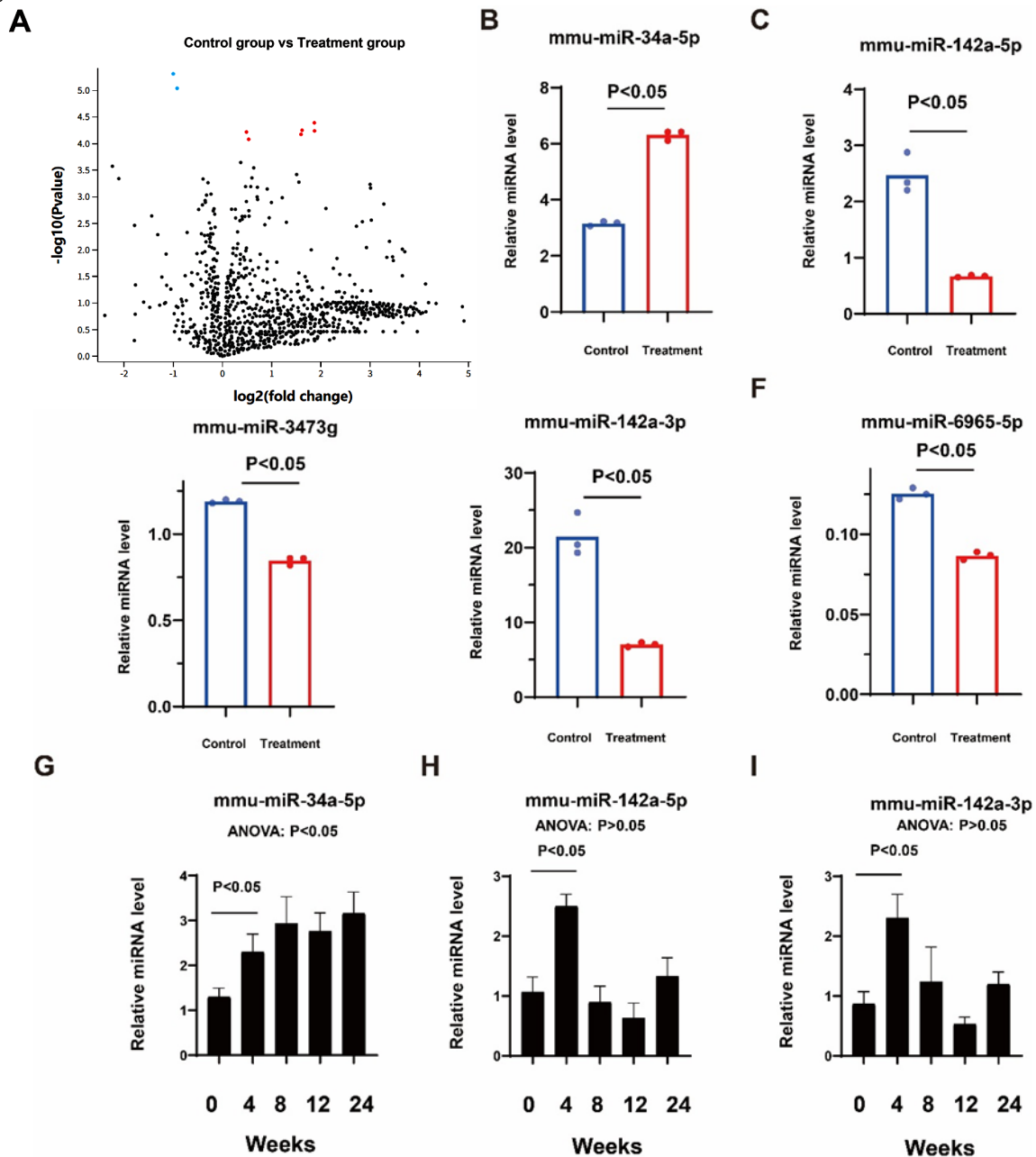


**Figure 2.** Identification of dis-regulated miRNAs in response to RILI in mice by using GEO public datasets. **(A)** Volcano plot analysis displaying the dis-regulated miRNAs in GEO public datasets GSE202586; The plot was calculated and drawn by GEO2R. **(B-F)** Expression values of **(B)** miR-34a-5p; **(C)** miR-142a-5p; **(D)** miR-3473g; **(E)** miR-142a-3p; and **(F)** miR-6965-5p between RILI mice and control group described in GSE202586. The plot was calculated and drawn by GEO2R. **(G-I)** RILI mice were constructed, and the expression values of miR-34a-5p, miR-142a-5p and miR-142a-3p in tissues were determined in indicated timepoint within 24 weeks post-irradiation.

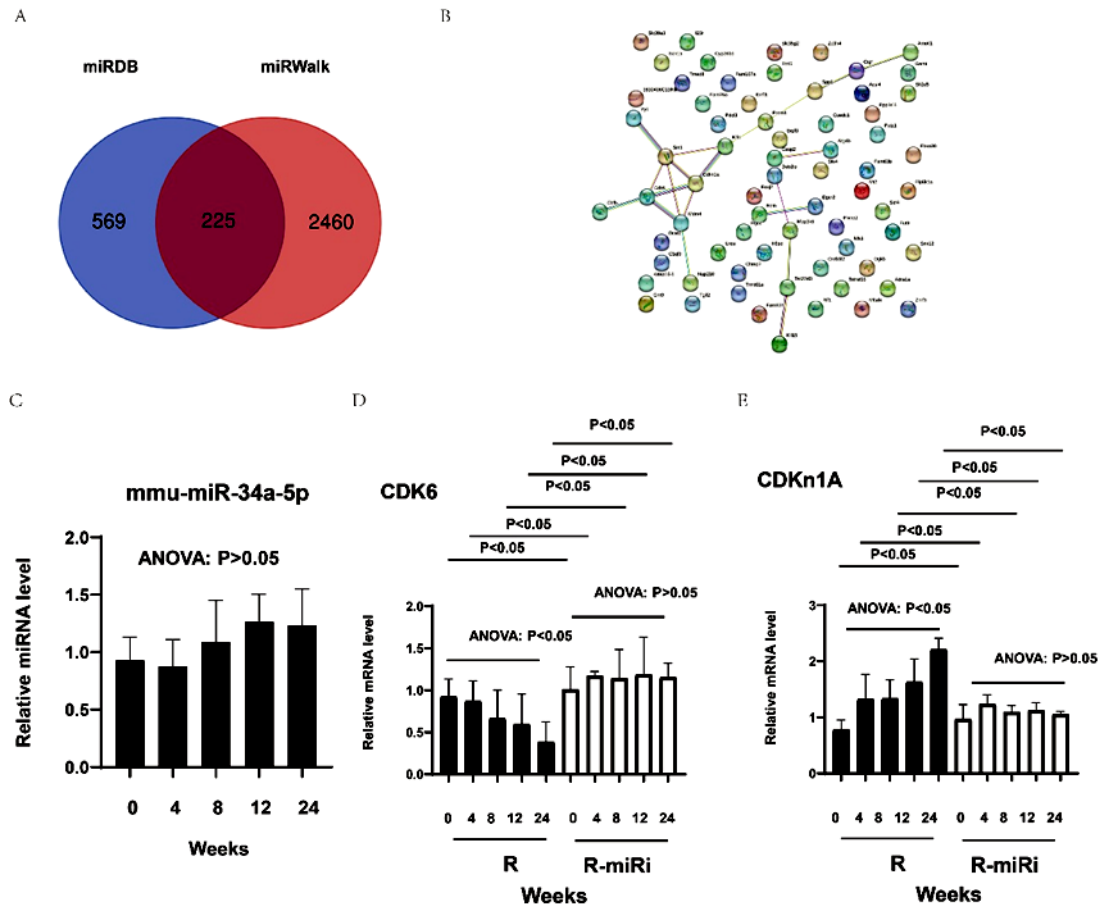


**Figure 3.** Identification of miR-34a potential targets and miR-34a involved PPI network. (A) Venn diagram showing the overlapped miR-34a's targets identified by miRDB and miRWalk; (B) Protein-protein interaction network among the identified transcripts described in figure 1E, and the miR-34a's targets described in figure 3A. The plot was calculated and drawn by STRING. (C-E) RILI mice were randomly allocated into R Group and R-miRi Group, and the expression values of miR-34a-5p, CDK6 and CDKn1A in tissues were determined in indicated timepoint within 24 weeks post-irradiation.

**Table 3.** Statistical characteristics & of the top ten differentially expressed miRNAs in GSE202586 dataset.

miRNA symbol	log (fold change)	t	P.Value	B
mmu-miR-34a-5p	-1.0013	-26.12	0.00000486	3.5993
mmu-miR-142a-5p	1.8677	16.14	0.00004055	2.61834
mmu-miR-3473g	0.4882	14.74	0.00006036	2.36847
mmu-miR-142a-3p	1.5974	14.4	0.00006677	2.30162
mmu-miR-6965-5p	0.5323	13.7	0.00008304	2.15253
mmu-miR-340-5p	0.3707	10.88	0.00022589	1.38974
mmu-miR-107-5p	-2.2376	-10.47	0.00026648	1.25201
mmu-miR-7050-5p	0.6358	10.3	0.00028569	1.19306
mmu-miR-150-5p	1.5073	9.63	0.00038138	0.94274
mmu-miR-202-3p	0.5977	9.3	0.00044184	0.81181

&: "statistical characteristics" was calculated by student t test, by comparing the control group and treatment,group. The control group includes three lung samples harvested 48 h after 0 Gy treatment; The treatment group includes three lung samples harvested 48 h after 8 Gy treatment.

**In-vivo determination of the effect of miR-34a/CDK6 axis on RILI mouse survival**

We employed a RILI mouse model to examine the impact of the miR-34a/CDK6 axis on RILI mouse survival. Within 24 weeks post-irradiation, the mortality rate in the R group was 62.5%, while none of the mice in the R-miRi group succumbed, indicating that the miR-34a inhibitor effectively prevented RILI-induced death. The mortality rate for the R-miRi-Ci group was 50% (4/8), suggesting that CDK6 siRNA counteracted the protective effect of the miR-34a inhibitor against RILI-induced death (figure

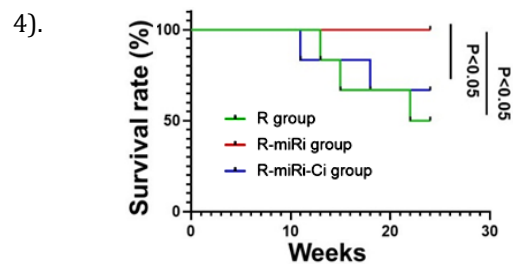


**Figure 4.** In-vivo determination the effect of miR-34a/CDK6 axis on survival of RILI mice. RILI mice were randomly allocated into R Group, R-miRi Group and R-miRi-Ci Group with indicated treatment, and the survival rates were determined within 24 weeks after RILI construction.

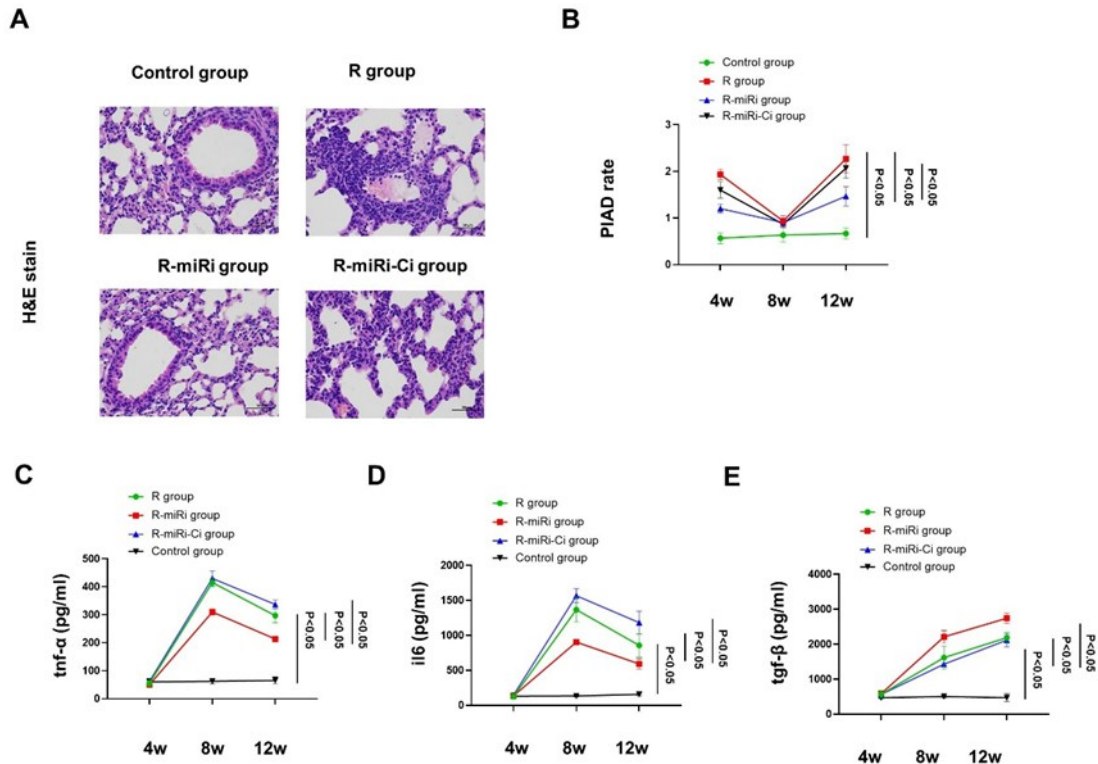


**Figure 5.** In-vivo determination the effect of miR-34a/CDK6 axis on RILI induced lung injury. RILI mice were randomly allocated into R Group, R-miRi Group and R-miRi-Ci Group with indicated treatment. **(A)** Representative mice lung histological samples of the above groups at 4 weeks after RILI construction (HE,  $\times 400$ ). **(B)** PIADs were determined within 12 weeks after RILI construction. **(C-E)** the serum **(C)**  $\text{tnf-}\alpha$ , **(D)**  $\text{il6}$  and **(E)**  $\text{tgf-}\beta$  were determined within 12 weeks after RILI construction.

#### In-vivo determination of the effect of miR-34a/CDK6 axis on RILI

To evaluate the pathological changes in lung injury, we assessed the severity of injury at various timepoints (figure 4A). Acute inflammation was observed in the radiation groups (R) at four weeks post-radiation (figure 4A). However, the R-miRi group displayed reduced inflammatory damage compared to the R group, suggesting that miR-34a-inhibitor treatment significantly mitigated RILI development in mice. The protective effect of the miR-34a-inhibitor was counteracted by CDK6 inhibitor treatment (figure 4A, R-miRi-Ci group vs R-miRi group).

At four weeks post-radiation, PIAD was elevated in the R group compared to the control. This value decreased in the R-miRi group relative to the R group, while PIAD increased in the R-miRi-Ci group compared to the R-miRi group. At eight weeks post-radiation, no significant differences were detected among the R, R-miRi, and R-miRi-Ci groups. However, by 12 weeks post-radiation, a significant distinction emerged among the three groups, mirroring the findings at four weeks post-radiation (figure 5B). Despite varying trends over time, serum levels of  $\text{TNF-}\alpha$ ,  $\text{IL-6}$ , and  $\text{TGF-}\beta$  in the R-miRi group were consistently lower than those in the R group. Conversely, the R-miRi-Ci group exhibited higher expression levels than the R-miRi group (figure 5C-E). Collectively, these results demonstrated that

the miR-34a inhibitor could attenuate RILI progression, while CDK6 siRNA negated this protective function of miR-34a.

## DISCUSSION

RILI results from radiation damage (15-16). Recently, numerous research groups have focused on identifying potential RILI regulatory factors. For example, Lei et al. synthesized previous findings, highlighting GSTP1 as a novel target in RILI (17). Li et al. demonstrated that NVP-AUY922 could alleviate RILI through the inhibition of ferroptosis (18). While these studies provide insight into RILI pathogenesis, a comprehensive understanding of the molecular regulatory network of RILI remains elusive.

Recent advancements in genomics have empowered researchers to uncover novel regulatory roles in various diseases. The establishment of publicly available databases for RNA-seq or microarray data has facilitated data mining, enabling the discovery of new molecular mechanisms underlying specific diseases (19). Integrating data from multiple platforms can theoretically improve result accuracy by minimizing the influence of samples or the platform itself (19-21). This approach has proven effective in several instances; for example, Wu et al. identified key genes associated with brain metastasis in breast cancer through a

comprehensive analysis of two microarray datasets, GSE125989 and GSE100534<sup>(20)</sup>. Furthermore, Zhen Liu et al. found that SLAMF8 and LILRB4 could serve as potent indicators for pulmonary tuberculosis by analyzing the overlapping targets of GSE20050, GSE57275, and GSE52819<sup>(21)</sup>. In this study, we conducted a comprehensive analysis of GSE202586 and GSE14431 using a Venn diagram. We found that the dysregulated genes in RILI exhibited significant variation between the two datasets, suggesting that different radiation doses and exposure durations may cause substantial pathological differences. Among the two datasets, we identified 10 overlapping genes (shown in tables 1-2), indicating their consistent expression across varying severity levels and duration of onset. These genes could be considered as being highly associated with RILI.

In our study, we utilized a comprehensive bioinformatics approach in conjunction with mouse model experiments to confirm that the miR-34a/CDK6 axis serves as a key regulatory mechanism in the development of RILI. It is well-established that RILI is closely linked to macrophage function. Macrophages can differentiate into either pro-inflammatory (M1) or anti-inflammatory (M2) phenotypes<sup>(22)</sup>. M1-polarized macrophages typically secrete TNF- $\alpha$  and IL-6, both of which are strongly implicated in RILI progression<sup>(5)</sup>. In contrast, TGF- $\beta$  is a key marker for M2 polarization<sup>(22)</sup>. Our findings revealed that miR-34a-inhibitor treatment led to decreased levels of TNF- $\alpha$  and IL-6 while simultaneously inducing TGF- $\beta$  expression. These effects were reversed by CDK6 siRNA, suggesting that the miR-34a/CDK6 axis modulates RILI progression by influencing macrophage M1/M2 polarization. This novel discovery is supported indirectly by previous reports. For instance, miR-34a has been shown to be highly expressed in M1 macrophages and to promote inflammation, oxidative stress, and M1 polarization<sup>(23)</sup>. Additionally, Qi et al. reported that miR-34a may directly enhance pulmonary fibrosis, a key characteristic of RILI<sup>(13)</sup>. CDK6, a known target of miR-34a, has been identified as a potential anti-inflammatory factor<sup>(14)</sup>. Birnhuber et al. demonstrated that CDK6 inhibition could increase pulmonary inflammatory infiltration and contribute to the induction of lung fibrosis<sup>(24)</sup>.

Another significant aspect of our findings is the close relationship between RILI-associated genes (listed in tables 1-2) and the miR-34a/CDK6 axis. For example, CDKN1A, a cyclin-dependent kinase inhibitor, is known to function through direct binding with CDK6<sup>(25)</sup>. Similar mechanisms have been reported for SIRT1<sup>(26)</sup> and MDM4<sup>(27)</sup>, among others. This suggests that the miR-34a/CDK6 axis interacts with multiple downstream signaling pathways, thereby orchestrating a systemic regulation of RILI pathogenesis and progression.

## CONCLUSION

Our results indicate that targeting the miR-34a/CDK6 axis may represent a promising therapeutic strategy for the treatment of RILI.

## ACKNOWLEDGEMENTS

None.

**Funding:** This work was supported by the Youth cultivation project of PLA (21QNPHY118).

**Conflict of interest:** The authors declare no conflict of interest.

**Ethics approval and consent to participate:** The mice-based study has been approved by the ethics committee of Eighth Medical Center of Chinese People's Liberation Army (PLA) General Hospital (ethics number: 309202111081149; ethics date: 08-11-2021). All authors declare that they have consented for publication.

**Authors' contributions:** All authors contributed equally to the design of the study, data collection and analysis, and the writing of the manuscript. All authors read and approved the final manuscript.

## REFERENCES

- Arroyo-Hernández M, Maldonado F, Lozano-Ruiz F, et al. (2021) Radiation-induced lung injury: current evidence. *BMC Pulm Med*, **21**(1): 9.
- Roy S, Salerno KE, Citrin DE (2021) Biology of Radiation-Induced Lung Injury. *Semin Radiat Oncol*, **31**(2):155-61.
- Hanania AN, Mainwaring W, Ghebre YT, et al. (2019) Radiation-Induced Lung Injury: Assessment and Management. *Chest*, **156**(1): 150-62.
- Li X, Chen J, Yuan S, et al. (2022) Activation of the P62-Keap1-NRF2 pathway protects against Ferroptosis in radiation-induced lung injury. *Oxid Med Cell Longev*, 8973509.
- Bao P, Zhao W, Mou M, Liu X (2020) MicroRNA-21 mediates bone marrow mesenchymal stem cells protection of radiation-induced lung injury during the acute phase by regulating polarization of alveolar macrophages. *Transl Cancer Res*, **9**(1): 231-9.
- Vaneechoutte D and Vandepoel K (2019) Curse: building expression atlases and co-expression networks from public RNA-Seq data. *Bioinformatics*, **35**(16): 2880-81.
- Ma L, Ye Y, Lu H, et al. (2022) A study on the radiosensitivity of radiation-induced lung injury at the acute phase based on single-cell transcriptomics. *Front Immunol*, **13**: 941976.
- Li H, Fu X, Guo H, et al. (2022) Sevoflurane reverses cisplatin resistance in neuroblastoma cells through the linc00473/miR-490-5p/AKT1 axis. *Saudi Med J*, **43**(11): 1209-16.
- Li Y, Zou L, Chu L, et al. (2021) Identification and Integrated Analysis of circRNA and miRNA of Radiation-Induced Lung Injury in a Mouse Model. *J Inflamm Res*, **14**: 4421-31.
- Zhou Y, Zhou B, Pache L, et al. (2019) Metascape provides a biologist-oriented resource for the analysis of systems-level datasets. *Nat Commun*, **10**(1): 1523.
- Szklarczyk D, Gable AL, Nastou KC, et al. (2021) The STRING database in 2021: customizable protein-protein networks, and functional characterization of user-uploaded gene/measurement sets. *Nucleic Acids Res*, **49**(D1): D605-12.
- Chen Y and Wang X (2020) miRDB: an online database for prediction of functional microRNA targets. *Nucleic Acids Res*, **48**(D1): D127-31.
- Sticht C, De La Torre C, Parveen A, Gretz N (2018) miRWalk: An online resource for prediction of microRNA binding sites. *PLoS One*, **13**(10): e0206239.

10. Sun Y, Du YJ, Zhao H, *et al.* (2016) Protective effects of ulinastatin and methylprednisolone against radiation-induced lung injury in mice. *J Radiat Res*, **57**(5): 505-511.
11. Jiang Y, You F, Zhu J, *et al.* (2019) Cryptotanshinone Ameliorates Radiation-Induced Lung Injury in Rats. *Evid Based Complement Alternat Med*, **2019**: 1908416.
12. Chen S, Ding R, Hu Z, *et al.* (2020) MicroRNA-34a Inhibition Alleviates Lung Injury in Cecal Ligation and Puncture Induced Septic Mice. *Front Immunol*, **11**: 1829.
13. Qi Y, Zhao A, Yang P, *et al.* (2020) miR-34a-5p Attenuates EMT through targeting SMAD4 in silica-induced pulmonary fibrosis. *J Cell Mol Med*, **24**(20): 12219-24.
14. Sun F, Fu H, Liu Q, *et al.* (2008) Downregulation of CCND1 and CDK6 by miR-34a induces cell cycle arrest. *FEBS Lett*, **582**(10): 1564-8.
15. Zhang Z, Zhou J, Verma V, *et al.* (2021) Crossed Pathways for Radiation-Induced and Immunotherapy-Related Lung Injury. *Front Immunol*, **12**: 774807.
16. Türkkän G, Willems Y, Hendriks LEL, *et al.* (2021) Idiopathic pulmonary fibrosis: Current knowledge, future perspectives and its importance in radiation oncology. *Radiother Oncol*, **155**: 269-77.
17. Lei X, Du L, Yu W, *et al.* (2021) GSTP1 as a novel target in radiation induced lung injury. *J Transl Med*, **19**(1): 297.
18. Li L, Wu D, Deng S, *et al.* (2022) NVP-AUY922 alleviates radiation-induced lung injury via inhibition of autophagy-dependent ferroptosis. *Cell Death Discov*, **8**(1): 86.
19. Zoabi Y and Shomron N (2021) Processing and analysis of RNA-seq data from public resources. *Methods Mol Biol*, **2243**: 81-94.
20. Wu W and Zheng L (2022) Comprehensive analysis identifies COL1A1, COL3A1, and POSTN as key genes associated with brain metastasis in patients with breast cancer. *Evid Based Complement Alternat Med*, **2022**: 7812218.
21. Zhao G, Luo X, Han X, Liu Z (2020) Combining bioinformatics and biological detection to identify novel biomarkers for diagnosis and prognosis of pulmonary tuberculosis. *Saudi Med J*, **41**(4): 351-60.
22. Wang D, Lin Y, Xu F, *et al.* (2022) SIRPα maintains macrophage homeostasis by interacting with PTK2B kinase in Mycobacterium tuberculosis infection and through autophagy and necroptosis. *EBioMedicine*, **85**: 104278.
23. Zhu H, Lin Y, Liu Y (2021) miR-34a increases inflammation and oxidative stress levels in patients with necrotizing enterocolitis by downregulating SIRT1 expression. *Mol Med Rep*, **24**(3): 664.
24. Birnhuber A, Egemnazarov B, Biasin V, *et al.* (2020) CDK4/6 inhibition enhances pulmonary inflammatory infiltration in bleomycin-induced lung fibrosis. *Respir Res*, **21**(1): 167.
25. Luyckx E, Van Leuven W, Andre D, *et al.* (2018) Loss of neuroglobin expression alters Cdkn1a/Cdk6-expression resulting in increased proliferation of neural stem cells. *Stem Cells Dev*, **27**(6): 378-390.
26. Iwagami Y, Zou J, Zhang H, *et al.* (2018) Alcohol-mediated miR-34a modulates hepatocyte growth and apoptosis. *J Cell Mol Med*, **22**(8): 3987-3995.
27. Portman N, Milioli HH, Alexandrou S, *et al.* (2020) MDM2 inhibition in combination with endocrine therapy and CDK4/6 inhibition for the treatment of ER-positive breast cancer. *Breast Cancer Res*, **22**(1): 87.